Wide Dynamic Range Sensing with Single Quantum Dot Biosensors

Stacey R. Opperwall, Anand Divakaran, Elizabeth G. Porter, Jeffrey A. Christians, Andrew J. DenHartigh, and David E. Benson*

Department of Chemistry & Biochemisty, Calvin College, 1726 Knollcrest Circle SE, Grand Rapids, Michigan 49546, United States

ABSTRACT

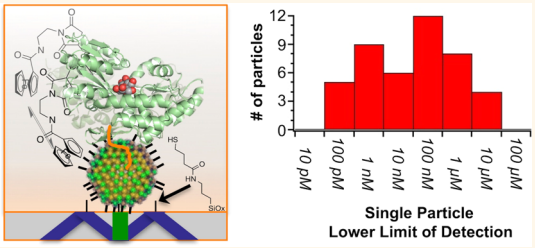

Single-particle analysis of biosensors that use charge transfer as the means for analyte-dependent signaling with semiconductor nanoparticles, or quantum dots, was examined. Single-particle analysis of biosensors that use energy transfer show analyte-dependent switching of nanoparticle emission from off to on. The charge-transfer-based biosensors reported here show constant emission, where the analyte (maltose) increases the emission intensity. By monitoring the same nanoparticles under various conditions, a single charge-transfer-based biosensor construct (one maltose binding protein, one protein attachment position for the reductant, one type of nanoparticle) showed a dynamic range for analyte (maltose) detection spanning from 100 pM to 10 μM while the emission intensities increase from 25 to 175% at the single-particle level. Since these biosensors were immobilized, the correlation between the detected maltose concentration and the maltose-dependent emission intensity increase could be examined. Minimal correlation between maltose detection limits and emission increases was observed, suggesting a variety of reductant-nanoparticle surface interactions that control maltose-dependent emission intensity responses. Despite the heterogeneous responses, monitoring biosensor emission intensity over 5 min provided a quantifiable method to monitor maltose concentration. Immobilizing and tracking these biosensors with heterogeneous responses, however, expanded the analyte-dependent emission intensity and the analyte dynamic range obtained from a single construct. Given the wide dynamic range and constant emission of charge-transfer-based biosensors, applying these single molecule techniques could provide ultrasensitive, real-time detection of small molecules in living cells.

KEYWORDS: single-molecule analysis · biosensors · quantum dots · hole transfer · charge transfer · dark state · particle tracking

Biosensors that use water-soluble CdSe core/ZnS shell (CdSe@ZnS) nanoparticles provide long-term microscopic evaluation of biological phenomena.[1] Of the analytes targeted by nanoparticle-based biosensors, small molecules present greater difficulty for biosensor design since a ligand–biomolecule binding event must somehow modulate a change in the nanoparticle fluorescence. Nanoparticle-based small-molecule biosensors link small-molecule-induced protein conformation changes to alter emission from the CdSe nanoparticle core using protein-pendant fluorophores or redox-active molecules (Figure 1A).[1,2] The pendant fluorophore or redox-active molecule is moved closer to or further from the nanoparticle surface to alter the amount of energy transfer or charge transfer with the CdSe core. Charge-transfer methods increase the photostability of these biosensors since energy transfer methods use less photostable organic dyes. Energy-transfer methods provide uniform responses that scale with average distance between and orientation of chromophores,[3] based on Förster-like dipolar coupling.[2,3] Charge-transfer methods scale with an exponential distance dependence[4–6] and, therefore, should be substantially more influenced by an ensemble of quencher–nanoparticle surface interactions rather than only distances. Analyte-dependent changes in nanoparticle emission intensity, therefore, arise from changes in these ensembles of quencher–nanoparticle interactions. Despite the photostability advantage of charge-transfer-based biosensors, the modest analyte-dependent changes in quantum dot emission intensities[7–10] have minimized the development of these biosensors as fluorescence microscopy probes. Examining single charge-transfer-based biosensors will show that the heterogeneity of nanoparticle emission response compares to energy transfer-based biosensors.

Single CdSe@ZnS nanoparticle emissions from energy-transfer-based and charge-transfer-based biosensors should differ substantially. Maltose biosensors based on maltose binding protein-appended CdSe@ZnS nanoparticles are well-studied[1,2] and are the basis for comparison. For energy-transfer-based biosensors at the single-particle level,

* Address correspondence to dbenson@calvin.edu.

Received for review June 15, 2012 and accepted August 19, 2012.

Published online August 27, 2012
10.1021/nn303347k

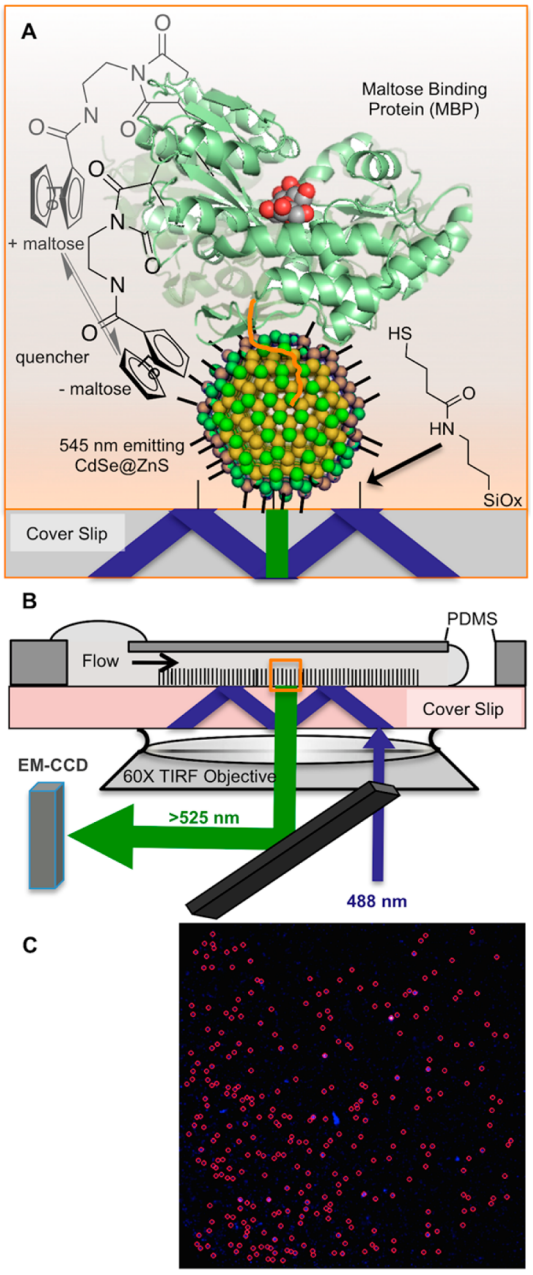

Figure 1. Biosensor system and experimental setup for single-molecule detection. (A) Cartoon of ferrocene-modified maltose binding protein adsorbed to mercaptohexadecanoate-capped CdSe@ZnS nanoparticles where maltose binding changes the protein conformation and alters the ferrocene–nanoparticle surface binding equilibrium. (B) Flow cell configuration with a silanized, thiol-terminated monolayer microscope slide (see Methods) with nanoparticle-based biosensors chemisorbed, covered by a polydimethylsiloxane (PDMS) slab with a 100 μM channel and a well on each side. The flow cell is situated on top of an inverted microscope with a total internal reflected fluorescence objective. (C) Averaged fluorescence intensity image from a 5 min acquisition with single nanoparticles identified by red circles.

similar maltose binding constants have been observed compared to bulk fluorescence for Cy3-modified maltose binding protein (MBP)-appended CdSe@ZnS nanoparticles.[11] This result showed that, on average, the maltose-driven conformational change of MBP was the same for MBP alone compared to MBP appended to CdSe@ZnS nanoparticles in bulk and at the single-molecule level. Two nanoparticle populations were observed: one population with non-emissive ("dark state") nanoparticles and a second population with emissive nanoparticles, relative to the MBP-appended Cy3 emission.[11] Maltose addition did increase the emissive state population with a 2-fold increased response relative to bulk measurements. Variations in the percent of dark state nanoparticles are known, in addition to energy transfer, to occur upon MBP binding to dihydrolipoic acid (DHLA)-capped CdSe@ZnS nanoparticles[11,12] and as a function of solution pH for streptavidin-linked CdSe@ZnS nanoparticles from Invitrogen.[13,14] In contrast, charge-transfer-based changes in CdSe emission intensity from electrochemical modulation[15] and dye adsorption[16] do not seem to correlate with dark state population. One report specifically used hole transport to an adsorbed reductant and observed the formation of bright and "gray" states with minimal dark state formation.[16] Formation of gray states provides continuous emission to detect nanoparticle biosensors in the quenched state and in the non-quenched state at the single-particle level. These studies suggest that the single-particle behavior of charge-transfer-based biosensors should be different than energy-transfer-based biosensors.

Charge transfer is different in nanoparticle biosensors compared to dye-adsorbed and electrochemically modulated nanoparticles. Biosensor systems incorporate an analyte-dependent method to reversibly move a protein-pendent reductant functional group close to and away from the nanoparticle surface (Figure 1A). This situation is different than surface-adsorbed dyes,[16] where one or more oxidant/reductant molecules per nanoparticle are adsorbed to the nanoparticle surface most of the time. Spectroelectrochemical studies are also different from biosensors[15] since electrons at a particular electrochemical potential are continuously transferred to or from the nanoparticle surface. Charge-transfer-based biosensors have, typically, one "adsorbate" molecule being dynamically associated with the nanoparticle surface where analyte–biomolecule binding alters the adsorbed/desorbed equilibrium (Figure 1A). Since ligand–biomolecule binding alters the adsorption equilibrium of a single reductant, the small changes in emission intensity are not surprising. With the heterogeneous surfaces of semiconductor nanoparticles, analyte-induced charge-transfer-based emissive responses should also be heterogeneous. In this study, we employ a novel tracking method that allows the same biosensors to be examined under a variety of conditions to directly address heterogeneous emission responses expected in charge-transfer-based biosensors.

RESULTS

Maltose binding protein (MBP) has been engineered to control charge transport between semiconductor nanoparticles and reductants depending on the concentration of maltose.[7,17] These systems have multiple components that can be easily altered: type of semiconducting nanoparticle,[18] biomolecular sensor,[18−20] reductant/quencher attached to MBP, reductant/quencher MBP attachment point,[7,17] and nanoparticle attachment domain.[21] In this report, we adapt a classic system (Figure 1) to enforce charge, potentially hole, transport from a photoexcited CdSe@ZnS nanoparticle to the MBP-pendant quencher, ferrocene. Hole transport was specifically selected due to gray state emission,[16] so that both the ligand-bound and ligand-free states are both observable at the single-particle level. A pentahistidine domain was used as the MBP−nanoparticle linkage (Figure 1A) for better comparison to biosensors that use energy transfer[11] as the reporting mechanism. A series of nucleic acid point mutations were used to confer cysteine side chain replacements at previously reported amino acid positions in MBP (Figure 1). *N*-(2-Ferrocene ethyl)maleimide[22] (**1**) was used for charge transport rather than (tetraammine)(5-maleimido-1,10-phenanthroline)ruthenium dication.[7,8,23] The ferrocene quencher was employed to increase ease of preparation[22] and because the electronic structure of ferrocene[24] shows no possibility of photoluminescence at room temperature or photoexcited electron transfer to the CdSe conduction band, thus suggesting exclusive charge transport *via* hole transport from the CdSe@ZnS nanoparticle to the MBP-attached ferrocene. More generally, a charge-transfer mechanism is consistent with ferrocene electrochemistry[25,26] since only an oxidative wave is observed within the potential window of CdSe[27] and around the potential of surface electron acceptor states.[8] Additionally, ferrocene-appended oligonucleotides are employed to study guanine-mediated hole transport.[28] These quencher−MBP−CdSe@ZnS nanoparticle systems are linked to the maltose-induced conformation change of MBP in order to alter quencher−CdSe@ZnS nanoparticle surface interactions. When the quencher in this system is ferrocene derivative **1**, the concentration of maltose provides a means to alter the emission intensity and, potentially, the amount of charge transport from photoexcited CdSe@ZnS nanoparticles.

Examining a variety of **1**-MBP-His_6 attachment positions found N282C MBP-His_6 to provide the system with the largest maltose-dependent change in nanoparticle emission intensity. These ferrocene−MBP−CdSe@ZnS nanoparticle systems were assembled as before,[7,17,21] where mercaptohexadecanoate-capped CdSe@ZnS nanoparticles (560 nm emitting) were incubated with 1 equiv of **1**-attached MBP-His_6 for 90 min. Binding was followed as a decrease in emission at 560 nm (N282C, 30%; F92C, 47%; N95C, 10%) and

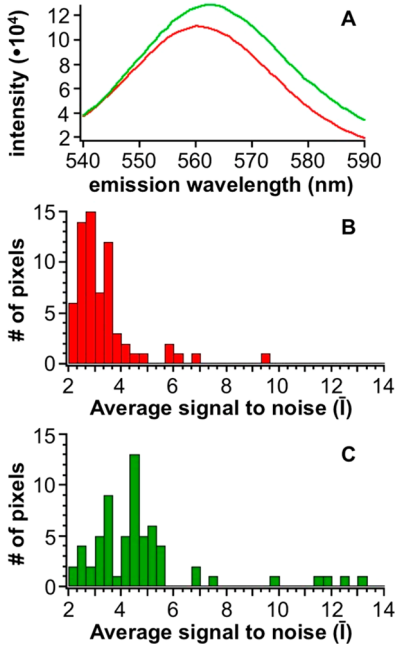

Figure 2. Maltose-dependent change in nanoparticle emission intensity for the nanoparticle-based biosensor system (1-modified N282C MBP-His_6, MHDA-capped CdSe@ZnS nanoparticles). (A) Bulk emission spectra with no maltose (red) and 100 μM maltose (green). Single-particle emission intensity histograms are shown for (B) no maltose and (C) 100 μM maltose.

shown to provide saturated MBP-His_6 binding to CdSe@ZnS nanoparticles. The system with quencher **1** attached to cysteine 282 (N282C MBP-His_6) provided the largest maltose-dependent restoration of emission (N282C, 15%; F92C, 10%; N95C, 7%) at 560 nm (Figure 2A). The emission quenching and maltose-induced changes are noticeably lower than systems using (tetraammine)(5-maleimido-1,10-phenanthroline)-ruthenium dication. Peptide-derived biosensors with ferrocene derivatives do not quench CdSe@ZnS nanoparticle emission,[8] where quenching is observed in ferrocene-appended chemosensors[29] and the biosensors detailed here. Similar differences were observed with ferrocene-appended CdSe@ZnS nanoparticles (substantial quenching)[30,31] compared to ferrocene-associated nanoparticles[32] (no quenching). To examine these inconsistencies under our aqueous conditions, (dimethyl)aminomethyl ferrocene was titrated against MHDA-capped CdSe@ZnS nanoparticles at pH 7.5, where the tertiary amine is protonated and positively charged. A Stern−Volmer quenching constant of 1×10^7 M^{-1} (Supporting Information) was consistent with quenching reported for this ferrocene−nanoparticle complex. Therefore, the difference between (tetraammine)(phenanthroline)ruthenium-derived and ferrocene-derived biosensors is the decreased excited state lifetime, potential for photoinduced electron transfer, and accessibility of the electron-donating orbitals in ferrocene.[24] Despite the small change in maltose-dependent emission

intensities, **1** was used as the quencher so that charge transport would be the primary mechanistic consideration and increase the ease of reagent preparation.

Fifty to 100 single biosensors were examined under various maltose concentrations using a combination of surface immobilization chemistries, micrometer scale channel fabrication, total internal reflected fluorescence, and image analysis software. So that the same biosensors were imaged under different conditions, the nanoparticles were immobilized on a thiol-terminated monolayer on a glass surface within a 100 μm by 100 μm polydimethylsiloxane (PDMS) channel (Figure 1B). Areas of the channel that were 2−3 cm below the inlet reservoir, having the highest density of single biosensors, were surveyed using total internal reflected fluorescence (TIRF) microscopy (Olympus 60× TIRF objective, 488 nm excitation). TIRF microscopy videos were acquired over 5 min and analyzed for pixels that contained a single biosensor. Cylindrical Gaussian emission intensity distributions were assumed to indicate a single biosensor immobilized in the area detected by one pixel, given the low bulk biosensor concentration (50 pM) used in the immobilization process. Background signals and noise were determined for each pixel in each frame using the intensities from pixels that formed a 5 pixel diameter circle surrounding the pixel in question. Emission intensity time trajectories were expressed as signal-to-noise ratios, and pixels that had signal-to-noise greater than 3.0 for more than 1.0 s were selected for evaluation. Signal-to-noise normalization was used to minimize detector variation since dual emission intensities, available to energy transfer measurements, were unavailable in this system for ratiometric reporting. Time trajectories of signal-to-noise ratios from selected pixels were recorded and referenced to the *x-y* coordinates from the detector array.

Single-particle analysis of maltose biosensing showed emission intensity increases with minimal initial dark state formation. The surface of nanoparticles and/or nanoparticle biosensors were illuminated for 10 min to stabilize emission responses, followed by video collection, sample introduction, and subsequent video collection. For a typical surface examined, 30−100 pixels were identified to contain a single nanoparticle (Figure 1C). Maltose-dependent changes in single-particle emission confirmed emission intensity increases with minimal initial dark state formation. Blinking analysis of these nanoparticles followed a power law dependence,[33] but unfortunately, no observed maltose-dependent differences were observed. Single-particle emission intensity analysis occurred from examining the average signal-to-noise values from a 5 min emission intensity trajectory ($\bar{I}$) before and after adding a maltose concentration (100 μM) that saturates MBP binding (Figure 2B,C). While the number of emitting single particles was unchanged (66 to 63),

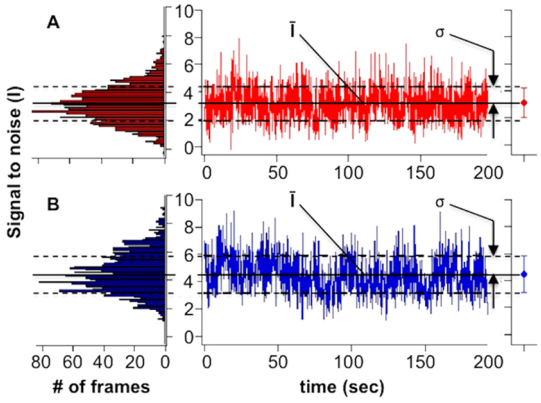

Figure 3. Emission intensity *versus* time trajectories (center), intensity histograms (left), and the $\bar{I}$ (solid line, point on right) and σ metrics (dashed line, error bars on right) for a single particle at 10 pM (A) and 100 μM maltose (B).

the emission intensity increased (mean $\bar{I}$ = 2.0 to 3.5; median $\bar{I}$ = 2.6 to 4.0). The emission intensity distributions could form a Poisson distribution but at least show a large heterogeneity in emission response. Single nanoparticle tracking from video to video, under various maltose concentrations, was used to address the heterogeneous nanoparticle emission response.

Referencing the detector *x-y* coordinates to each nanoparticle emission time trajectory allowed the same emissive single nanoparticle to be tracked and monitored under a variety of conditions. Single nanoparticles exhibited similar emission intensities over at least 24 video acquisitions that took between 5 and 10 min (~3 h). This allowed the charge-transfer-based maltose biosensor system to be interrogated under maltose concentrations ranging from 10 pM to 100 μM. In addition to the mean signal-to-noise ratio ($\bar{I}$) for each intensity−time trajectory, the standard deviation (σ) of the signal-to-noise ratios was determined (Figure 3). At a given maltose concentration (or other condition), three videos were acquired to generate three trajectories, $\bar{I}$s, and σs for each biosensor, if detected. The average and standard deviation of the three mean intensities, denoted avg($\bar{I}$) and $\sigma(\bar{I})$, were used to see if a significant emission intensity increase occurred with increasing maltose concentrations. Blank samples with just water-soluble CdSe@ZnS nanoparticles and biosensor systems without **1** generated no significant change in emission intensities with the addition of maltose (Supporting Information). Likewise, no significant emission intensity change was noted when the full biosensor system was exposed to successive buffer additions. Furthermore, the pH of the buffer was altered from pH 9 (50 mM tetraborate) to pH 6 (50 mM phosphate), which yielded no significant change in emission intensities, while only a slight decrease in number of emitting single nanoparticles (15% decrease from pH 9 to 6). These observations suggest that the detection and reporting methods for

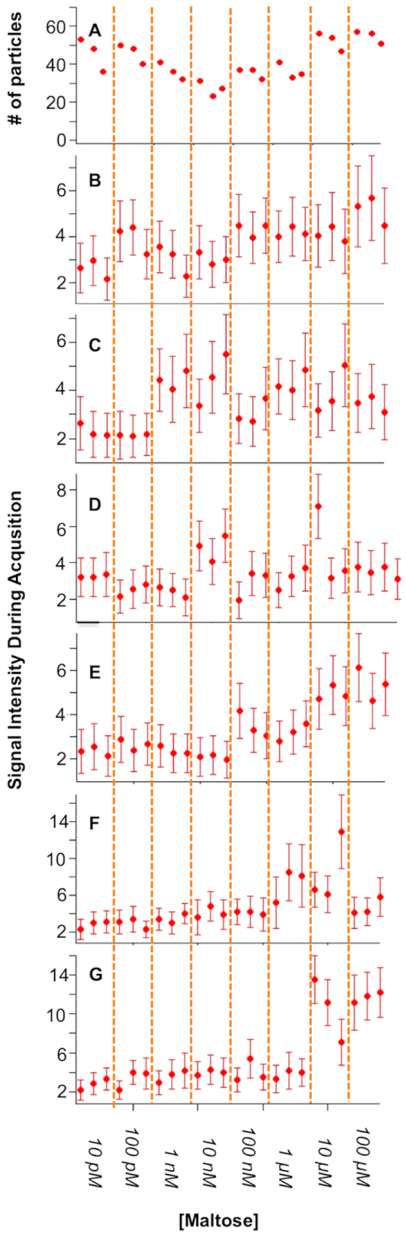

Figure 4. Maltose-dependent changes for the same single-nanoparticle-based biosensor's emission intensity. (A) Number of emissive nanoparticles detected per experiment. (B–G) Maltose-dependent changes in single biosensor emission ($\bar{I}$, σ as error bars) with a single nanoparticle lower limit of detection (spLOD) of 100 pM (B), 1 nM (C), 10 nM (D), 100 nM (E), 1 μM (F), and 10 μM (G).

single-nanoparticle TIRF microscopy with these biosensors are robust.

Heterogeneous emission responses for the single charge-transfer-based biosensors were observed over a wide maltose concentration range. In contrast to biosensors that use energy transfer, a relatively constant number of emitting single nanoparticles was observed from 10 pM to 100 μM maltose (Figure 4A). As observed in bulk emission and uncorrelated single-particle analysis (Figure 2), the initial emission intensity of charge-transfer-based biosensors was lower compared to after maltose exposure (Figure 4B–G). Individual intensity–time trajectories were classified by the avg($\bar{I}$) and $\sigma(\bar{I})$ metrics to determine for a single biosensor what maltose concentration gave a significant increase in nanoparticle emission intensity from the previous maltose concentration. Single-particle examples are provided in Figure 4B–H, where each particle shows a significant increase in avg($\bar{I}$), based on $\sigma(\bar{I})$, upon the introduction of a higher maltose concentration. The wide range of maltose concentrations that caused an increase in emission intensity was termed the single-particle lower limit of detection (spLOD). The spLOD classification for each particle (43) was obtained through visual inspection, rather than automated analysis, to ensure proper single-particle assignment.

Emission intensity changes and maltose concentrations associated with the spLOD were heterogeneous and uncorrelated but, when combined, reproduce the bulk emission response. The spLODs and emission intensity changes were tabulated for each particle. The observed spLODs spanned 6 orders of magnitude in maltose concentration, as shown by the histogram in Figure 5A. The center of the maltose spLOD distribution is between 100 nM and 1 μM, consistent with the known dissociation constants (K_D or $1/K_A$) for maltose binding to MBP.[7] The maltose-dependent emission intensity increases also showed heterogeneous responses (Figure 5B). No correlation between the heterogeneous maltose-dependent emission increase and the maltose spLOD was observed (Figure 5C). The Poisson distribution in the spLOD *versus* emission intensity suggests heterogeneous interactions/charge transport to provide maltose-dependent emission intensity increases. In order to compare these results to bulk emission properties, a bulk titration curve was reconstructed (Figure 5D) based on the maltose-dependent emission increases (Figure 5C) at various maltose spLODs (Figure 5B). The reconstructed maltose titration curve roughly approximates those titration curves previously reported,[7,17] where the reconstructed curve is broader than others, reflecting the observed heterogeneous maltose affinities. Taken together, single-particle tracking and analysis shows a heterogeneous maltose-dependent emission response that approximates bulk fluorescence properties and with a wide dynamic range of maltose detection.

DISCUSSION

Observation of heterogeneous emission responses at the single-particle level was made possible by the methods used to track the same immobilized nanoparticles across experiments. Classic single-nanoparticle emission experiments yielded no significant maltose-dependent change in emission properties besides the emission intensity histograms in Figure 2. By examining a set of the same nanoparticles under a variety of conditions, the maltose-dependent emission

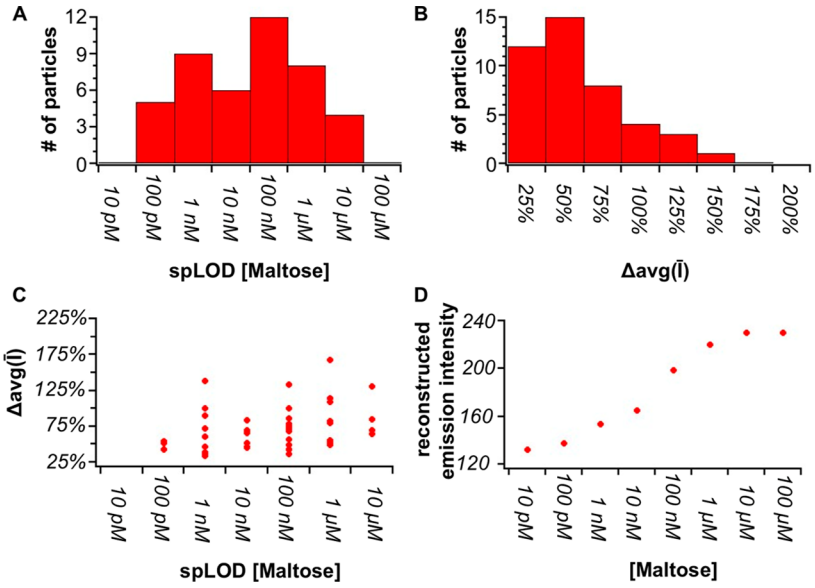

Figure 5. Analysis of single-nanoparticle-based biosensor emission responses to maltose. (A) Histogram of maltose single-particle lower limit of detection (spLOD). (B) Histogram of percent maltose-dependent increase (Δavg($\bar{I}$)) in nanoparticle emission intensity. (C) Correlation of percent emission increase with maltose spLOD. (D) Reconstructed maltose titration curve from maltose-dependent emission intensities combined with maltose spLODs.

response for each biosensor could be examined. A number of reporting metrics were examined to classify nanoparticles, but the average emission intensity ($\bar{I}$) and standard deviation (σ) of the emission intensity over 5 min provided the most reliable and accessible metric. Correlating the $\bar{I}$ and σ of the same nanoparticle from observation to observation allowed further assessment (avg($\bar{I}$) and $\sigma(\bar{I})$) and comparison between different conditions. No significant change in the ratio of emitting ("on") to non-emitting ("off") nanoparticles was observed when the pH, conductivity, or maltose concentration was varied. Using the avg($\bar{I}$) and $\sigma(\bar{I})$ metrics, the maltose concentration at the onset of significant increase in avg($\bar{I}$) showed that quantitative information can be derived from this heterogeneous emission response if the same nanoparticle is tracked from experiment to experiment. The heterogeneous nanoparticle emission response was found to be two-fold: in maltose concentration responses (spLOD, Figure 5A) and percent emission increases (%Δavg($\bar{I}$), Figure 5B). These two heterogeneous responses were found to be independent of each other using the nanoparticle tracking method.

Heterogeneous emission responses of charge-transfer-based biosensors on the single-particle level are consistent with recent reports.[15,16] Compared to single-particle studies of an energy-transfer-based biosensor that uses MBP,[11] the emission intensity from each nanoparticle varied as analyte bound to single charge-transfer-based biosensors, rather than changing the dark state population as in the energy-transfer-based biosensors. Dye-adsorbed CdSe nanoparticles also saw multiple emission intensities from the same nanoparticle and attributed the intermediate emission (gray states) to a hole dissociated state.[16] Similar gray-to-on state transitions are seen for this system, where the gray states could be formed by hole dissociation to the pendant ferrocene derivative **1**. Upon maltose addition, the emission intensities of the **1**-modified nanoparticles increased, suggesting that **1** is moved on average further away from the nanoparticle surface after charge recombination but before charge dissociation occurs again. Maltose addition showed no significant change in power law dependence, bulk emission lifetimes, or dark state population for the **1**-modified nanoparticles. It is worth noting that these observations are consistent with the recent finding of hole-transfer-quenched nanoparticles (type B) whose emission intensity is not correlated with emission lifetime and power law behavior.[15] Taken together, these charge-transfer-based biosensors have emission properties consistent with a hole-transfer mechanism.

Heterogeneous maltose-dependent emission responses are consistent with different MBP conformations being stabilized by different nanoparticle surfaces. The heterogeneous surface of nanoparticles is well-recognized. Electrophoretic measurements have ensured one **1**-appended MBP is attached per CdSe@ZnS nanoparticle (Supporting Information), which suggests that the heterogeneous emission response comes from the heterogeneous surface of CdSe@ZnS nanoparticles and MBP attachment orientation. The protein literature has shown that stabilization of one conformation over another will alter the small-molecule binding equilibrium. For example, amino acid substitutions at the MBP domain–domain interface can vary the native maltose–MBP affinity (K_A = 1.4 × 10^6 M^{-1}, K_D = 700 nM) from 1.4 × 10^8 M^{-1} (K_D = 7.4 nM) to 500 M^{-1} (K_D = 1.8 mM).[34] We infer that different maltose affinities arise

from a variety of MBP conformations stabilized by different nanoparticle surfaces to form a six decade-wide spLOD distribution. Futhermore, each **1**-MBP nanoparticle had a different charge-transfer efficiency (25 to 175% increase in maltose-dependent emission intensity) suggestive of different MBP-mediated interactions between **1** and the nanoparticle surface. Such heterogeneous emission responses should be expected based on the 100 mV midpoint and over 100-fold electron transfer rate variations for a Cy5-modified azurin to a modified gold surface.[35] The heterogeneities were most pronounced for low protein coverage, as in our system. MBP conformational exchange kinetics further complicate this picture, where the maltose-bound MBP conformation only exists around 100 ms at any given maltose concentration.[36] While these charge-transfer-based biosensors were developed with photoinduced electron transfer in metalloproteins in mind,[37,38] charge/hole transfer in these biosensors is much more reliant on the electron transfer to and from materials.[15,16]

The heterogeneous responses reported here are, actually, ideal for single-molecule analysis using nanoparticle-based biosensors. Slide immobilization does allow this system to be integrated with microfluidics for maltose quantitation, where a set of maltose standards could be applied to a set of single immobilized nanoparticles followed by sample introduction. Once calibrated, one nanoparticle-based biosensor system can increase the dynamic range from two decades[17] to six decades of analyte concentration. The single-biosensor analysis also provides spLODs that are two to three decades lower than bulk measurements. Finally, a marginal 15% increase in bulk fluorescence intensity upon maltose addition increased up to 175% at the single-particle level. Besides microfluidic applications, this technique could eventually be applied to nanoparticle tracking in live cell imaging to provide qualitative, ultratrace analyte detection. For example, if the 100 pM spLOD is applied to an average size HeLa cell (4000 μm^3, 4 fL), the detection limit would be 250 maltose molecules per cell. Given the modularity of charge-transport-based biosensors,[7,18−20,39] this could open up detection of small-molecule metabolites or toxins before or during the onset of diseased states. Given these constraints, charge-transfer-based biosensors have significant advantages to energy-transfer-based biosensors for single-particle analysis.

Heterogeneous responses of charge-transfer-based biosensors display the material nature of these biosensors and provide an efficient means for implementing these sensors to real-time single-cell fluorescence analysis. Localization and/or tracking these charge-transfer-based biosensors throughout the experiment allows fluorescence responses over six decades of maltose concentration starting at 100 pM and substantially increased emission responses from bulk solution. Extrapolation to the single-cell level would suggest that these biosensors could detect a specific small molecule at a level of less than 1000 molecules per cell. More specific reductant-nanoparticle surface interactions could be designed to minimize this heterogeneity, but until then, this heterogeneity coupled with nanoparticle tracking provides wide dynamic range biosensing to systems with modest bulk emission biosensing properties.

METHODS

Biosensor Assembly. All reagents, unless noted, were used without additional purification. Hydrophobic 560 nm emitting CdSe nanoparticles coated with 2−3 monolayers of ZnS were obtained from NNLabs (Fayetteville, AK). These nanoparticles were rendered water-soluble with stable bulk emission by exchange with mercaptohexadecanoic acid, deprotonation with potassium *t*-butoxide, and extensively rinsed with pH 7.5 50 mM 3-(*N*-morpholino)propanesulfonic acid (MOPS) buffer *via* an ultrafiltration centrifugal filter (Millipore Ultracel-10) as reported previously.[7] *Escherichia coli* maltose binding protein was mutagenized by standard recombinant DNA techniques and purified by amylose affinity chromatography as previously reported.[21] *N*-(2-Ferrocene ethyl)maleimide (**1**) was synthesized and purified to 99% purity (NMR and HPLC) based on previous literature reports.[22] Surface cysteine MBPs (N282C, F92C, and N95C) were modified with **1** using similar conditions as modification with (tetraammine)(5-maleimido-1,10-phenanthroline)-ruthenium(II) bis(hexafluorophosphate) previously.[7] The **1**-modified MBPs with a six histidine tag on the carboxy termini were assembled onto MHDA-capped, ZnS-coated, CdSe nanoparticles (CdSe@ZnS) as reported before[21,40] and confirmed to have one **1**-appended MBP bound per CdSe@ZnS nanoparticle.

Slide Immobilization. Microscope coverslips (1.5) were cleaned, rinsed, and modified to form an amine-terminated monolayer (VectaBond, Vector Laboratories). These coverslips were incubated in aqueous dithiobis[succinimidyl propionate] (DSP, Thermo), rinsed, and air-dried. Polydimethylsiloxane (Dow Corning) slabs were polymerized on master templates to form a single 100 μm by 100 μm channel, terminated with two reservoirs, and were adhered to derivatized coverslips. The channels were filled and incubated with a 10 mM tricarboxyethylphosphine (TCEP, Thermo) aqueous solution to produce a thiol-terminated monolayer on the glass surface. Flow was established with syringe suction and maintained by gravity. Once the phosphine solution was rinsed from the channel, a 50 pM solution of biosensors in pH 7.5 buffered solution (50 mM tris(hydroxymethyl)aminomethane, 100 mM NaCl) was rinsed and incubated in the channel.

Bulk Fluorescence Analysis. A Spex Fluorolog-3 fluorometer was used for bulk fluorescence analysis with a 1 s integration time and 3 nm slit widths. Solutions (1 mL) of each biosensor were examined at 25 °C (1− 2 min equilibration time) with constant stirring (Cuv-o-Stir; Hellma). Maltose concentration was increased by adding 1−5 μL aliquots of maltose stock solutions (100 nM to 100 mM) followed by 2−5 min equilibration.

Single-Nanoparticle Fluorescence Analysis. Microscope slides were mounted on the stage of an Olympus IX71 inverted fluorescence microscope. A 60× oil immersion objective (NA 1.45) for total internal reflected fluorescence (PlanApoN UIS2, Olympus) was used to selectively illuminate surface species with 488 nm light from an argon ion laser (65 mW, IMA1, Melles Griot, Carlsbad, CA) with a FITC filter cube (49011, Chroma Technology Group, Bellows Falls, VT). Fluorescence images were collected

with an Andor iXon^{em}+ electron multiplication CCD (South Windsor, CT) and cooled at −100 °C. Fluorescence videos were taken using programs in LabView (National Instruments, Austin, TX), IDL (Exelis, Boulder, CO), and MatLab (MathWorks, Natick, MA) obtained from Dr. David Rueda (Wayne State University). The initial programs were modified to identify pixels that potentially contain single nanoparticles and minimize background noise. Briefly, pixels that were the maxima of a Gaussian distribution of emission intensity were saved as pixel intensities (pI_{max}) *versus* time, average pixel intensities of a 5 pixel radius circle surrounding the intensity maxima pixel (I_{bkg}) *versus* time, pixel *x*-*y* coordinates, and a variety of additional metrics. The background signal ($\bar{I}_{bkg}$) was assumed to follow a five-point linear interpolation of the $pI_{background}$ signal. A signal-to-noise ratio was then calculated as

$$I = (pI_{max} - \bar{I}_{bkg})/\sigma_{bkg} \quad (1)$$

where I is the signal-to-noise ratio and σ_{bkg} is the standard deviation of I_{bkg} subtracted from $\bar{I}_{bkg}$. Pixels that had a signal-to-noise ratio greater than or equal to 3 for more than 2 s over a 5 min emission trajectory were saved for further analysis. Time trajectories of signal-to-noise ratios were then characterized as the average signal-to-noise ratio, $\bar{I}$, and the standard deviation of the signal-to-noise ratio, $\sigma(\bar{I})$, for each nanoparticle. For each nanoparticle, trajectories and parameters were indexed with *x*-*y* coordinates from the CCD. Tracking a nanoparticle from video to video was performed by a searching for nanoparticles within 3 pixels in each direction of each other from different videos. A file containing the addresses and parameters of a nanoparticle over all videos was generated for each nanoparticle. Final data collection and analysis was performed in IgorPro (WaveMetrics, Lake Oswego, OR).

Analysis of Single-Particle Maltose Detection. Plots of $\bar{I}$ for each video, with σ reported as error bars, were generated for maltose titration experiments (Figure 4). Three videos were recorded at each maltose concentration, where the resultant $\bar{I}$ values were averaged, avg($\bar{I}$), and standard deviations taken, $\sigma(\bar{I})$. For each particle, plots of $\bar{I}$ for each video were visually inspected where the first significant increase, $\bar{I}_{previous} + \sigma(\bar{I}_{previous})$, was attributed to the lowest maltose concentration that particle detected (spLOD). The percentage of average emission intensities, %Δavg($\bar{I}$), was calculated from before and after initial maltose detection for each particle. A maltose titration curve as expected from bulk solution analysis was reconstructed either by applying spLOD and %Δavg($\bar{I}$) values as a step function and summing all particles (Figure 5D) or by summing all of the particle avg($\bar{I}$) values for each maltose concentration. Both plots were similar. Due to the lack of sampling around the maltose concentration close to the dissociation constant, a reconstructed maltose−MBP affinity was not calculated but is consistent with literature values (~700 nM).

Conflict of Interest: The authors declare no competing financial interest.

Acknowledgment. The authors gratefully acknowledge the support from Calvin College (DEB), Office of Naval Research (N00014810837), National Science Foundation (RUI-1058391, ARI-R2-0963433, and MRI-0923167), and from initial work and guidance on this system by Drs. P. Godakumbura, D. Gao, E. Aleman, and D. Rueda.

Supporting Information Available: Experimental results for Stern−Volmer titrations of CdSe@ZnS nanoparticles with (dimethyl)aminomethylferrocene at pH 7.5, pH-dependent responses of MHDA-capped CdSe@ZnS nanoparticles, buffer-dependent responses of **1**-MBP-attached CdSe@ZnS nanoparticles, maltose-dependent responses of MBP-attached CdSe@ZnS nanoparticles, and the distribution of MBP binding to CdSe@ZnS nanoparticles. This material is available free of charge *via* the Internet at http://pubs.acs.org.

REFERENCES AND NOTES

1. Algar, W. R.; Susumu, K.; Delehanty, J. B.; Medintz, I. L. Semiconductor Quantum Dots in Bioanalysis: Crossing the Valley of Death. *Anal. Chem.* **2011**, *83*, 8826–8837.
2. Benson, D. E. Reagentless Biosensors Based on Nanoparticles. In *Nanomaterals for Biosensing*; Nanomaterials for Life Sciences; Wiley Interscience: New York, 2006; Vol. 8, pp 337−367.
3. Medintz, I. L.; Konnert, J. H.; Clapp, A. R.; Stanish, I.; Twigg, M. E. A Fluorescence Resonance Energy Transfer-Derived Structure of a Quantum Dot-Protein Bioconjugate Nanoassembly. *Proc. Natl. Acad. Sci. U.S.A.* **2004**, *101*, 9612–9617.
4. Marcus, R. A.; Sutin, N. Electron Transfers in Chemistry and Biology. *Biochim. Biophys. Acta* **1985**, *811*, 265–322.
5. Vinayakan, R.; Shanmugapriya, T.; Nair, P. V.; Ramamurthy, P.; Thomas, K. G. An Approach for Optimizing the Shell Thickness of Core−Shell Quantum Dots Using Photoinduced Charge Transfer. *J. Phys. Chem. C* **2007**, *111*, 10146–10149.
6. Pelton, M.; Smith, G.; Scherer, N. F.; Marcus, R. A. Evidence for a Diffusion-Controlled Mechanism for Fluorescence Blinking of Colloidal Quantum Dots. *Proc. Natl. Acad. Sci. U.S.A.* **2007**, *104*, 14249–14254.
7. Sandros, M. G.; Gao, D.; Benson, D. E. A Modular Nanoparticle-Based System for Reagentless Small Molecule Biosensing. *J. Am. Chem. Soc.* **2005**, *127*, 12198–12199.
8. Medintz, I. L.; Pons, T.; Trammell, S. A.; Grimes, A. F.; English, D. S.; Blanco-Canosa, J. B.; Dawson, P. E.; Mattoussi, H. Interactions between Redox Complexes and Semiconductor Quantum Dots Coupled *via* a Peptide Bridge. *J. Am. Chem. Soc.* **2008**, *130*, 16745–16756.
9. Raymo, F. M.; Yildiz, I. Luminescent Chemosensors Based on Semiconductor Quantum Dots. *Phys. Chem. Chem. Phys.* **2007**, *9*, 2036–2043.
10. Callan, J.; Mulrooney, R.; Kamila, S.; McCaughan, B. Anion Sensing with Luminescent Quantum Dots—A Modular Approach Based on the Photoinduced Electron Transfer (PET) Mechanism. *J. Fluoresc.* **2008**, *18*, 527–532.
11. Pons, T.; Medintz, I. L.; Wang, X.; English, D. S.; Mattoussi, H. Solution-Phase Single Quantum Dot Fluorescence Resonance Energy Transfer. *J. Am. Chem. Soc.* **2006**, *128*, 15324–15331.
12. Pons, T.; Medintz, I. L.; Farrell, D.; Wang, X.; Grimes, A. F.; English, D. S.; Berti, L.; Mattoussi, H. Single-Molecule Colocalization Studies Shed Light on the Idea of Fully Emitting *versus* Dark Single Quantum Dots. *Small* **2011**, *7*, 2101–2108.
13. Durisic, N.; Wiseman, P. W.; Grütter, P.; Heyes, C. D. A Common Mechanism Underlies the Dark Fraction Formation and Fluorescence Blinking of Quantum Dots. *ACS Nano* **2009**, *3*, 1167–1175.
14. Durisic, N.; Godin, A. G.; Walters, D.; Grütter, P.; Wiseman, P. W.; Heyes, C. D. Probing the "Dark" Fraction of Core−Shell Quantum Dots by Ensemble and Single Particle pH-Dependent Spectroscopy. *ACS Nano* **2011**, *5*, 9062–9073.
15. Galland, C.; Ghosh, Y.; Steinbrück, A.; Sykora, M.; Hollingsworth, J. A.; Klimov, V. I.; Htoon, H. Two Types of Luminescence Blinking Revealed by Spectroelectrochemistry of Single Quantum Dots. *Nature* **2011**, *479*, 203–207.
16. Song, N.; Zhu, H.; Jin, S.; Lian, T. Hole Transfer from Single Quantum Dots. *ACS Nano* **2011**, *5*, 8750–8759.
17. Sandros, M. G.; Shete, V.; Benson, D. E. Selective, Reversible, Reagentless Maltose Biosensing with Core−Shell Semiconducting Nanoparticles. *Analyst* **2006**, *131*, 229–235.
18. Shete, V. S.; Benson, D. E. Protein Design Provides Lead(II) Ion Biosensors for Imaging Molecular Fluxes around Red Blood Cells. *Biochemistry* **2009**, *48*, 462–470.
19. Swain, M. D.; Octain, J.; Benson, D. E. Unimolecular, Soluble Semiconductor Nanoparticle-Based Biosensors for Thrombin Using Charge/Electron Transfer. *Bioconjugate Chem.* **2008**, *19*, 2520–2526.
20. Aryal, B. P.; Benson, D. E. Electron Donor Solvent Effects Provide Biosensing with Quantum Dots. *J. Am. Chem. Soc.* **2006**, *128*, 15986–15987.
21. Sandros, M. G.; Gao, D.; Gokdemir, C.; Benson, D. E. General, High-Affinity Approach for the Synthesis of Fluorophore Appended Protein Nanoparticle Assemblies. *Chem. Commun.* **2005**, 2832–2834.

22. Di Gleria, K.; Hill, H. A. O.; Wong, L. L. *N*-(2-Ferrocene-ethyl)-maleimide: A New Electroactive Sulphydryl-Specific Reagent for Cysteine-Containing Peptides and Proteins. *FEBS Lett.* **1996**, *390*, 142–144.
23. Trammell, S.; Goldston, H. M.; Tran, P. T.; Tender, L. M.; Conrad, D. W.; Benson, D. E.; Hellinga, H. W. Synthesis and Characterization of a Ruthenium(II)-Based Redox Conjugate for Reagentless Biosensing. *Bioconjugate Chem.* **2001**, *12*, 643–647.
24. Lancaster, K. M.; Finkelstein, K. D.; DeBeer, S. Kβ X-ray Emission Spectroscopy Offers Unique Chemical Bonding Insights: Revisiting the Electronic Structure of Ferrocene. *Inorg. Chem.* **2011**, *50*, 6767–6774.
25. Ito, N.; Saji, T.; Aoyagui, S. Electrochemical Formation of Stable Ferrocene Anion and the Formal Rate Constant of the Ferrocene$^{0/-}$ Electrode. *J. Organomet. Chem.* **1983**, *247*, 301–305.
26. Winter, R. F.; Geiger, W. E. Electron-Transfer Properties of Cp*FeP_5: Evidence for Dimerization Reactions Following Both Oxidation and Reduction. *Organometallics* **1999**, *18*, 1827–1833.
27. Hagfeldt, A.; Graetzel, M. Light-Induced Redox Reactions in Nanocrystalline Systems. *Chem. Rev.* **1995**, *95*, 49–68.
28. Paul, A.; Bezer, S.; Venketramani, R.; Kocsis, L.; Wierzbinski, E.; Balaeff, A.; Keinan, S.; Beratan, D. N.; Achim, C.; Waldeck, D. H. Role of Nucleobase Energetics and Nucleobase Interactions in Single-Stranded Peptide Nucleic Acid Charge Transfer. *J. Am. Chem. Soc.* **2009**, 6498–6507.
29. Mulrooney, R. C.; Singh, N.; Kaur, N.; Callan, J. F. An "Off−On" Sensor for Fluoride Using Luminescent CdSe/ZnS Quantum Dots. *Chem. Commun.* **2009**, 686–688.
30. Dorokhin, D.; Tomczak, N.; Velders, A. H.; Reinhoudt, D. N.; Vancso, G. J. Photoluminescence Quenching of CdSe/ZnS Quantum Dots by Molecular Ferrocene and Ferrocenyl Thiol Ligands. *J. Phys. Chem. C* **2009**, *113*, 18676–18680.
31. Dorokhin, D.; Tomczak, N.; Han, M.; Reinhoudt, D N.; Velders, A. H.; Vancso, G. J. Reversible Phase Transfer of (CdSe/ZnS) Quantum Dots between Organic and Aqueous Solutions. *ACS Nano* **2009**, *3*, 661–667.
32. Impellizzeri, S.; Monaco, S.; Yildiz, I.; Amelia, M.; Credi, A.; Raymo, F. M. Reversible Phase Transfer of (CdSe/ZnS) Quantum Dots between Organic and Aqueous Solutions. *J. Phys. Chem. C* **2010**, *114*, 7007–7013.
33. Kuno, M.; Fromm, D. P.; Gallagher, A.; Nesbitt, D. J.; Micic, O. I.; Nozik, A. J. Fluorescence Intermittency in Single InP Quantum Dots. *Nano Lett.* **2001**, *1*, 557–564.
34. Marvin, J. S.; Hellinga, H. W. Manipulation of Ligand Binding Affinity by Exploitation of Conformational Coupling. *Nat. Struct. Mol. Biol.* **2001**, *8*, 795–798.
35. Salverda, J. M.; Patil, A. V.; Mizzon, G.; Kuznetsova, S.; Zauner, G.; Akkilic, N.; Canters, G. W.; Davis, J. J.; Heering, H. A.; Aartsma, T. J. Fluorescent Cyclic Voltammetry of Immobilized Azurin: Direct Observation of Thermodynamic and Kinetic Heterogeneity. *Angew. Chem., Int. Ed.* **2010**, *49*, 5776–5779.
36. Telmer, P. G.; Shilton, B. H. Insights into the Conformational Equilibria of Maltose-Binding Protein by Analysis of High Affinity Mutants. *J. Biol. Chem.* **2003**, *278*, 34555–34567.
37. Nocera, D. G.; Winkler, J. R.; Yocom, K. M.; Bordignon, E.; Gray, H. B. Kinetics of Intermolecular and Intramolecular Electron Transfer from Ruthenium(II) Complexes to Ferricytochrome *c*. *J. Am. Chem. Soc.* **1984**, *106*, 5145–5150.
38. Gray, H. B.; Winkler, J. R. Electron Flow through Proteins. *Chem. Phys. Lett.* **2009**, *483*, 1–9.
39. Medintz, I. L.; Farrell, D.; Susumu, K.; Trammell, S. A.; Deschamps, J. R.; Brunel, F. M.; Dawson, P. E.; Mattoussi, H. Multiplex Charge-Transfer Interactions between Quantum Dots and Peptide-Bridged Ruthenium Complexes. *Anal. Chem.* **2009**, *81*, 4831–4839.
40. Sapsford, K. E.; Pons, T.; Medintz, I. L.; Higashiya, S.; Brunel, F. M.; Dawson, P. E.; Mattoussi, H. Kinetics of Metal-Affinity Driven Self-Assembly between Proteins or Peptides and CdSe−ZnS Quantum Dots. *J. Phys. Chem. C* **2007**, *111*, 11528–11538.